#### **ORIGINAL PAPER**



# Image-based radiodensity profilometry measures early remodeling at the bone-callus interface in sheep

Tianyi Ren<sup>1</sup> · Karina Klein<sup>2</sup> · Brigitte von Rechenberg<sup>2,3</sup> · Salim Darwiche<sup>2,3</sup> · Hannah L. Dailey<sup>1</sup>

Received: 24 June 2021 / Accepted: 21 December 2021 © The Author(s), under exclusive licence to Springer-Verlag GmbH Germany, part of Springer Nature 2022

#### **Abstract**

Bone healing has been traditionally described as a four-phase process: inflammatory response, soft callus formation, hard callus development, and remodeling. The remodeling phase has been largely neglected in most numerical mechanoregulation models of fracture repair in favor of capturing early healing using a pre-defined callus domain. However, in vivo evidence suggests that remodeling occurs concurrently with repair and causes changes in cortical bone adjacent to callus that are typically neglected in numerical models of bone healing. The objective of this study was to use image processing techniques to quantify this early-stage remodeling in ovine osteotomies. To accomplish this, we developed a numerical method for radiodensity profilometry with optimization-based curve fitting to mathematically model the bone density gradients in the radial direction across the cortical wall and callus. After assessing data from 26 sheep, we defined a dimensionless density fitting function that revealed significant remodeling occurring in the cortical wall adjacent to callus during early healing, a 23% average reduction in density compared to intact. This fitting function is robust for modeling radial density gradients in both intact bone and fracture repair scenarios and can capture a wide variety of the healing responses. The fitting function can also be scaled easily for comparison to numerical model predictions and may be useful for validating future mechanoregulatory models of coupled fracture repair and remodeling.

Keywords Remodeling · Bone fracture healing · Micro-computed tomography · Tibia · Ovine osteotomy

### 1 Introduction

The fracture healing process is commonly described as a four-phase concept: inflammation phase, soft callus formation phase, hard callus formation phase, and bone remodeling phase (Claes et al. 2012; Pivonka and Dunstan 2012; Einhorn and Gerstenfeld 2015; Ghiasi et al. 2017). Numerical simulations have been used to predict mechanobiological processes in the regions of fracture healing. Numerous finite element (FE) models have been developed to analyze local mechanical responses to varying loading conditions

(Ament and Hofer 2000; Claes et al. 2002; Lacroix and Prendergast 2002; Shefelbine et al. 2005; Simon et al. 2011; Steiner et al. 2013, 2014; Wilson et al. 2017; Wang and Yang 2018; Pietsch et al. 2018; Ghiasi et al. 2019; Engelhardt et al. 2021). Such models have been used to study different factors that impact the healing process, for example the mechanics of the fixation hardware, or outcomes following inverse dynamization (Wehner et al. 2014; Wilson et al. 2017). Some studies have also emphasized that the initial phase of healing is critical for modeling of the healing process (Ghiasi et al. 2019). Recently, we applied a mechanoregulatory model of fracture healing to show that the rate of healing depends on the geometry of the fracture and that all fracture types experience a small healing delay with torsional instability (Ren and Dailey 2020). We also showed that modifying a strain-based mechanoregulatory model of fracture healing to include a geometric proximity function can successfully restrict callus formation to the region near the fracture line and achieve simulation domain independence (Schwarzenberg et al. 2021b).

Published online: 08 January 2022



Hannah L. Dailey hlr3@lehigh.edu

Department of Mechanical Engineering and Mechanics, Packard Laboratory, Room 556, Lehigh University, 19 Memorial Drive West, Bethlehem, PA 18015, USA

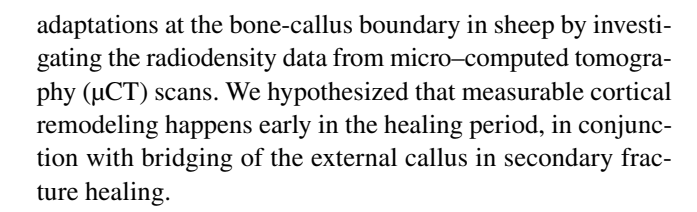
Musculoskeltal Research Unit (MSRU), Vetsuisse Faculty, University of Zurich, Zurich, Switzerland

<sup>&</sup>lt;sup>3</sup> Center for Applied Biotechnology and Molecular Medicine (CABMM), University of Zurich, Zurich, Switzerland

These techniques hold promise to predict outcomes under different mechanical or biological conditions and in response to new treatment strategies, but they all share a key limitation: the cortical wall is assigned static mechanical properties and included in the mechanical loading simulations, but it is excluded from the mechanoregulatory healing algorithms. These models neglect remodeling activity during fracture healing because this last stage of fracture healing is often described conceptually as having limited overlap with the repair phase. However, in vivo data suggest that remodeling of the cortical wall occurs concurrently with soft callus development and mineralization. For example, previous reports generated from nanoindentation testing have provided highly localized evidence of decreasing bone density in the radial direction through the cortical bone toward the callus (Manjubala et al. 2009; Preininger et al. 2011). This evidence indicates the remodeling phase of secondary bone fracture healing is associated with structural changes in both the callus and the adjacent cortical bone throughout the healing process and that these effects should be included in early-stage fracture repair models.

The key barrier to developing new mechanoregulatory models that can consider coupled repair and remodeling is the lack of available validation data. The validation strategy used for most recent mechanoregulation models has focused on the global structural mechanics of the limb and qualitative comparison of model predictions to histological analysis of tissue in the callus. For example, the assessment of a model's performance in predicting the spatial and temporal development of tissues in the callus is usually based on only the general trends of mechanical data (e.g., torsional rigidity) (Ren and Dailey 2020; Schwarzenberg et al. 2021b) or temporal data (e.g., bridging time, interfragmentary motion) (Lacroix and Prendergast 2002; Isaksson et al. 2006; Wehner et al. 2014; Pietsch et al. 2018). Ideally, the localized tissue composition and distribution should also be investigated to assess whether tissue growth and differentiation criteria within the algorithms are functioning correctly. The historical gold standard for assessing mechanical properties within tissue samples has been nanoindentation testing. This method has been used to probe the microscale properties of bone and callus and identify gradients in porosity and density (Manjubala et al. 2009; Preininger et al. 2011; Moramacías et al. 2017). However, these physical measurement techniques involve time-consuming destructive postmortem testing with specialized equipment and the resulting data cannot be obtained in vivo, or for large regions of tissue, or in large numbers of samples. Regrettably, these limitations mean that generalizable quantitative data describing remodeling across the cortical wall into callus does not currently exist.

Accordingly, the purpose of this study was to develop a numerical technique for quantifying structural remodeling



#### 2 Methods

## 2.1 Animal specimen information

Twenty-six adult female Swiss alpine sheep (2–3 years old, weighing 59–87 kg) were part of two previously completed research studies with two different tibial osteotomy models stabilized by medial plating (Schwarzenberg et al. 2021a). Group 1 consisted of data from twelve animals with a 17 mm tibia defect augmented with autografts and stabilized with a 13-hole stainless steel plate (broad straight veterinary 3.5 mm LCP, 172 mm in length, with 3.5 mm bicortical screws; DePuy Synthes®). Sheep in group 1 were sacrificed 12 weeks after surgery. Group 2 consisted of data from fourteen animals with a 3 mm gap tibia defect stabilized with a 12-hole stainless steel plate (broad straight veterinary 3.5 mm locking compression plate (LCP), 159 mm in length, with 3.5 mm bicortical screws; DePuy Synthes®). Sheep in group 2 were sacrificed 9 weeks after surgery. All experiments were conducted at the Musculoskeletal Research Unit in Zürich, Switzerland, according to the Swiss laws of animal protection and welfare and authorized by the local governmental veterinary authorities (License No. ZH 183/17).

# 2.2 Micro-computed tomography (µCT) scanning

After animal sacrifice, both intact and operated tibiae were excised, stripped of soft tissue, and all hardware was removed, taking care not to disrupt the callus. Samples were then wrapped in saline-soaked gauze, and  $\mu$ CT scanned using an XtremeCT II Micro-CT scanner (Scanco Medical AG, Bruettisellen, Switzerland) with an X-ray voltage of 68 kVp and X-ray current of 1470  $\mu$ A. The resulting scans had an isotropic resolution of 60.7  $\mu$ m.

# 2.3 Image segmentation

A region of interest (ROI) was selected at three different locations of each operated limb diaphyseal segment scan: 10 mm from the most proximal aspect of the tibia, 10 mm from the most distal aspect of the tibia, and just proximal to the fracture line at the level of maximum callus radius (Fig. 1). The midshaft ROI started with the first tomogram showing the complete cortical cross-sectional proximal to the osteotomy. The proximal and distal ROI were above and



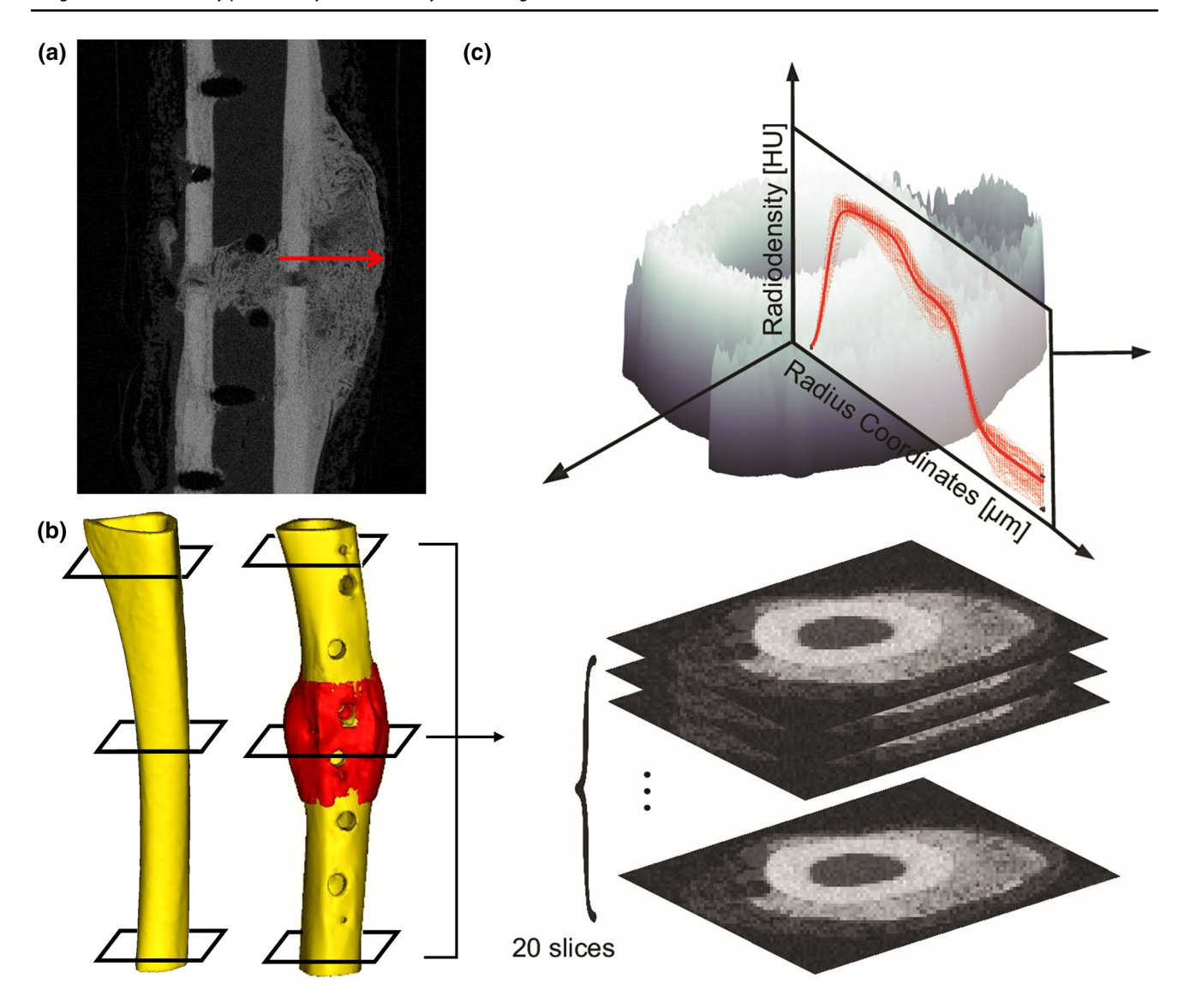


**Fig. 1** a Coronal slice view from a micro-CT scan of an ovine tibial osteotomy at 9 weeks post-op. In this study, radiodensity gradients were sampled in the direction indicated by the red arrow. **b** Three regions of interest (ROI) were identified for sampling in each intact

and each operated limb: proximal, distal, and at the level of the fracture.  $\mathbf{c}$  Each ROI consisted of 20 axial slices that were analyzed to measure radial radiodensity profiles in the cortical wall and callus region

below the most proximal and distal screw holes. Sampling slices from the intact limb were also taken at the corresponding levels. At each sampling location (region of interest), a total of 20 slices were selected for analysis.

An automated segmentation algorithm was developed in MATLAB 2021a (The MathWorks, Inc., Natick, Massachusetts, USA) to define the outer boundary of the callus as well as the area enclosed by the pericortical boundary of the preexisting cortical bone. The detailed workflow can be seen in Fig. 2. Post-segmentation data processing was carried out on all 2D tomograms located within each ROI. The process for segmentation of cortical bone and callus was based in part on previously reported methods (Buie et al. 2007; Morgan et al. 2009; Bissinger et al. 2017). To complete this task,

the algorithm required two initial estimates of the segmentation thresholds. The selection of these thresholds affects the cortical bone and callus boundaries of the output mask and requires subsequent refinement. First, the soft tissue region was excluded using connected-component labeling. Noise was then reduced by applying a median filter. Next, the original dataset was re-thresholded and masked with the detected boundaries of the bone-callus region. Dilation and erosion operations were then used to determine the bone and callus boundary. The initial estimates of the segmentation thresholds were then refined by minimization of spline energy to achieve smoothness of the detected tissue boundaries for each sheep. A locally convex boundary criterion was also used to correct any boundary defects caused by small



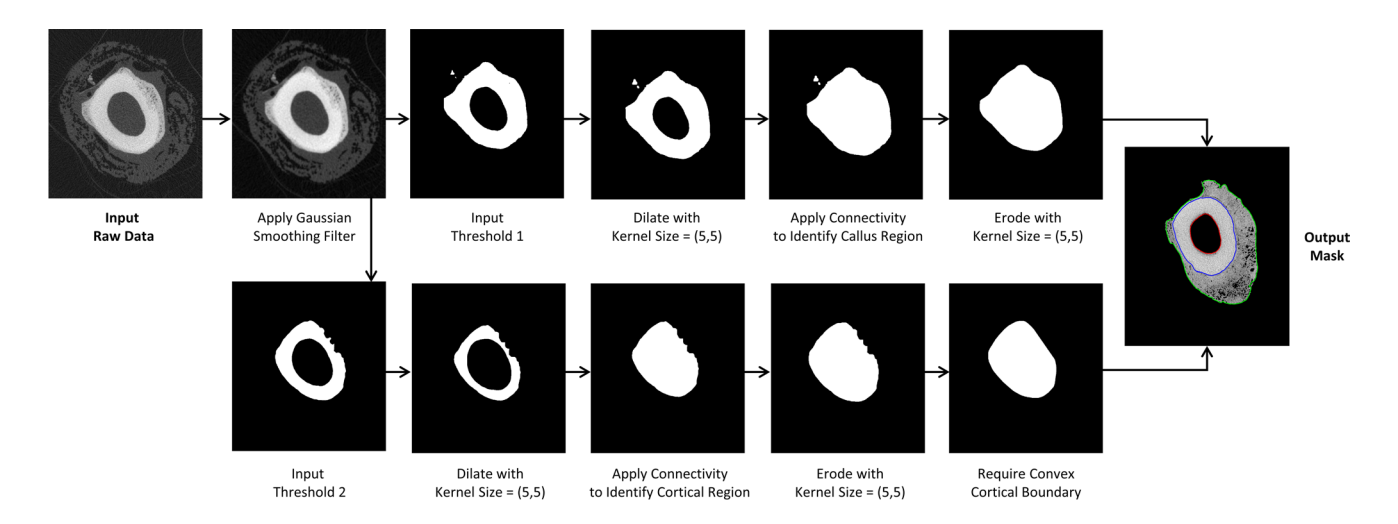


Fig. 2 Regions of cortical bone and callus were identified using an automated segmentation method developed in MATLAB 2021a. This method requires two global threshold inputs, which are used to ini-

tialize the splines that define the endosteal, pericortical, and callus boundaries, and subsequently refined as shown

regions of lower-density cortical bone. Finally, a mask of the callus, cortical bone, and non-bone regions was created by combining the output of the previous steps.

The slice extraction and segmentation processes were repeated at all three levels of height in both the intact and operated tibiae.

# 2.4 Radiodensity data sampling and curve fitting

The process for radiodensity sampling is illustrated in Fig. 3. In each 2D tomogram within the region of interest, the centroid of the cortical bone was calculated from the endocortical boundary (red boundary) in the mask geometry. A polar array of sampling lines was created in 1-degree increments throughout the entire 360-degree angle range, with each line having its origin at the centroid and extending through the cortical wall and callus. The radiodensity values along the profile lines were sampled in 60 µm increments in the radial direction, a distance equal to the in-plane resolution of the scan. Pixel data were retrieved from the grayscale image using a bicubic interpolation technique. Data quality was checked for each profile line and individual profile lines were excluded from the data set if the callus was not present or too thin (thickness smaller than 10 mm, measured in the radial direction along a profile sampling line). Radial sampling was repeated using the same procedure for all 20 slices in each ROI and pooled to create a point cloud that defined the radiodensity profile line for each ROI in each animal (Fig. 1c).

In this animal model, medial plating produced asymmetric callus formation, as can be clearly seen in Fig. 3c. Cortical wall thickness was also not constant across all radial profile lines. To enable a combined curve-fitting analysis of the profilometry samples from within each region of interest,

a registration and scaling procedure was defined to create a consistent dimensionless coordinate system for the cortical wall and for the callus, when present. Each profile line was registered to set its linear coordinate system to zero at the bone-callus boundary, or the pericortical boundary if intact. Negative linear coordinates corresponding to the cortical wall were normalized to the local cortex thickness of each profile line (Fig. 3c, d), such that r = -1 was the endocortical boundary and r = 0 was the pericortical boundary. For the positive linear coordinates, the normalization procedure depended on whether callus was present. For the intact limbs, positive coordinates were normalized to the local cortex thickness (Fig. 5b). For the operated limbs with callus, positive coordinates were normalized to the doubled local callus thickness, producing r = 0.5 at the outer boundary of the callus mask and ensuring data sampling beyond the callus into the soft tissue zone (Fig. 5c). The resulting average number of sampling points per region of interest was 170,340.

To enable comparisons between the treated and untreated limbs of all animals, the sampled radiodensity values were also normalized to the median cortical bone density of the intact diaphysis of each animal. Within each animal, all local radiodensity values sampled from the profile lines were normalized to this baseline median cortical bone density, regardless of limb (intact or operated) and ROI location (proximal, midshaft, and distal).

Curve fitting techniques were then used to mathematically model the collective radial density profile using the sampling points collected at each ROI. To develop an appropriate fitting function for measuring local structural changes, we started with the simplest case, an intact cortical wall fit with a double sigmoid function:



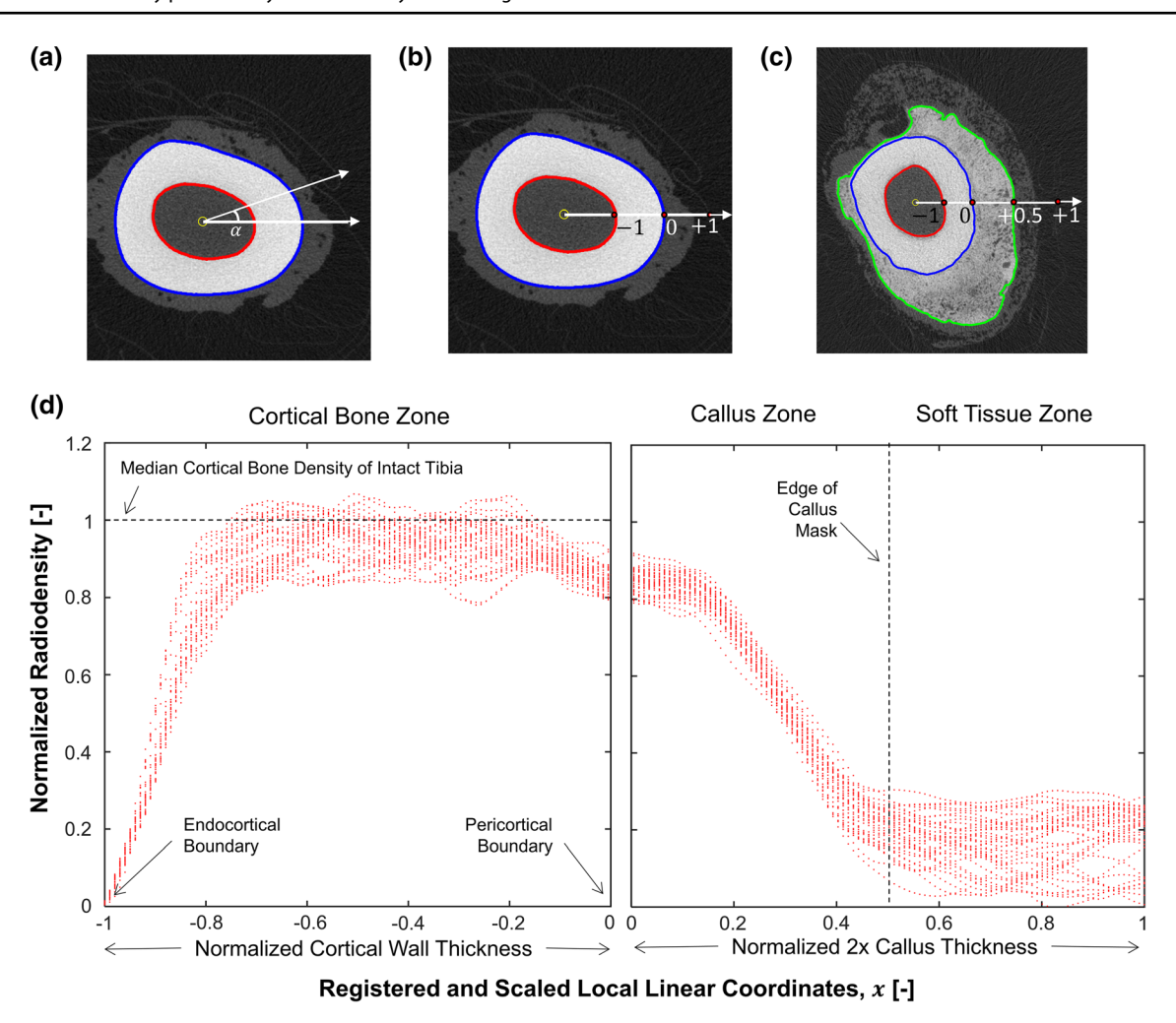


**Fig. 3** a A polar array of radial profile lines was created from the cortical centroid through the cortical wall and callus, if present, and radiodensity values were sampled from the underlying scan data. **b** For intact bones, each profile line was registered to set its linear coordinate system to zero at the pericortical boundary and sampling points were extended up to one cortical thickness into the surrounding soft

tissue.  $\mathbf{c}$  For samples with callus, profile lines were registered to zero at the bone-callus boundary and sampling points were extended to double the local callus thickness.  $\mathbf{d}$  Resulting compiled profilometry sampling data for one animal at the level of the callus in the operated limb. All radiodensity values were normalized to the median cortical bone density of the intact tibia for that animal

$$f(r) = \frac{1}{1 + e^{-a_1(r - b_1)}} * \frac{1}{1 + e^{-a_2(r - b_2)}}$$
(1)

where in general for a sigmoid function, the parameters a sets the width of the transition zone from a function value of 0 to a function value of 1, and the parameter b sets the center of this transition zone. The performance of the basic double sigmoid was critically evaluated using goodness of fit statistics and visual inspection, and additional logical and piecewise-defined terms were sequentially added in stages to improve the fit, as described in the Results below. Piecewise functions were always split at r=0, the normalized coordinate representing the pericortical boundary.

Two curve-fitting methods were used to obtain fitting parameters. The nonlinear least-squares method was implemented via the MATLAB Curve Fitting Toolbox (R2021a). In addition to this standard curve-fitting technique, a multi-objective optimization method was introduced to fit the parameters of piecewise-defined fitting functions. The additional constraints were introduced to preserve continuity of piecewise-defined functions at r=0, the pericortical boundary. These conditions included a requirement for position and slope continuity of as described in Eq. 2. This multi-objective optimization method can be formulated to find the coefficients of f(r), minimizing the residuals (sum of the squares), of all the data points:



$$\min_{a,b,g,d} \sum_{i=1}^{m} (y_i - f_{r<0}(r_i))^2$$

$$\min_{a,b,g,d,c} \sum_{k=1}^{n} (y_k - f_{r>0}(r_k))^2$$
s.t.  $f_{r<0}(0) - f_{r>0}(0) = 0$ 

$$f_{r<0}'(0) - f_{r>0}'(0) = 0$$

where  $r_i$  and  $r_k$  are the set of data points in the cortical wall or external to the cortical wall, n and m are the total number of data points of the cortical wall or the callus. The minimization problem was solved using the MATLAB Optimization Toolbox (R2021a).

Goodness of fit for all curve fits was evaluated using the resulting  $R^2$  values for all animals. Note that while linear regression-based curve fitting techniques can produce  $R^2$  with a significance level (p value) (Morgan et al. 2009; Freedman et al. 2018), nonlinear regression and optimization-based methods cannot and are typically reported with only the  $R^2$  (Preininger et al. 2011; Scheuren et al. 2020).

After the final fitting parameters were obtained for each sheep, the resulting fit function, f(r), was evaluated to calculate the slope at the bone-callus interface and quantify the extent to which remodeling had produced a smooth functionally graded interface at the bone-callus boundary. The radiodensity slope is the derivative of the fitting function at the bone callus boundary. For intact bone not bounded by callus, an additional custom MATLAB script was also used to calculate the average density value in the cortical wall plateau, which was reported as the mean cortical density of each fitted curve.

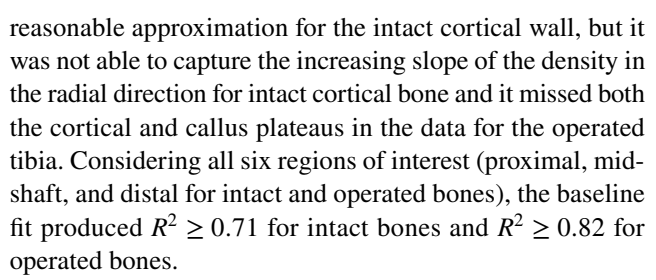
## 2.5 Statistical analysis

All statistical analyses were performed using SPSS Statistics 27 (IBM Corp; Armonk, New York, USA). A value of  $P\!=\!0.05$  was used as the threshold for statistical significance. A two-tailed paired-sample t test was used to analyze if the fitting function constants and the evaluated slope of the fitting function at the pericortical boundary were significantly different between the operated and contralateral limbs. A two-tailed unpaired samples t test was used to compare fitting parameters between the 3 mm and 17 mm osteotomy groups.

## 3 Results

# 3.1 Choice of curve fitting function

The fitting results of the baseline double sigmoid function (Eq. 1) are shown in Fig. 4a. This function provided a



Several alternative methods were then investigated and critically evaluated with respect to their ability to capture the essential features of the bone density profile curves. First, a logical linear term and a constant were added to the double sigmoid function of Eq. 1 to account for the observed nonzero density gradient in the cortical wall (r < 0) and nonzero background radiodensity:

$$f(r) = \frac{1}{1 + e^{-a_1(r - b_1)}} * \frac{1}{1 + e^{-a_2(r - b_2)}} + d + \begin{cases} cr \ r < 0 \\ 0 \ r \ge 0 \end{cases}.$$
(3)

where c is the linear slope applied only within the cortical wall and d is the background density constant. Adding a logical linear term and a constant (Eq. 3) produced a good fit with  $R^2 \ge 0.78$  for the intact bones, but this fitting function failed to capture the remodeling behavior evidenced by a decrease in density in the cortical wall at the bone callus boundary (Fig. 4b), with  $R^2 \ge 0.85$  for the operated bones.

To improve the fit for samples with callus, an additional sigmoid term was added using a logical constraint to restrict its application to radial coordinates external to the pericortical boundary  $(r \ge 0)$ :

$$f(r) = \begin{cases} \frac{1}{1 + e^{-a_1(r-b_1)}} * (g_1 + \frac{(1-g_1)}{1 + e^{-a_2(r-b_2)}}) + cr + d_1, \ r < 0\\ \frac{g_2}{1 + e^{-a_3(r-b_3)}} + d_2, \qquad \qquad r \ge 0 \end{cases}$$
(4)

where the constants  $g_1$  and  $g_2$  in the sigmoid terms allow for non-unity in the upper sigmoid plateau and the constants  $d_1$  and  $d_2$  allow for nonzero background radiodensity on both the internal and external bounds of the fitting function. In this piecewise definition, the cortical function (r < 0) is a generalized double logistic function, and the callus function is a single logistic function. The piecewise logistic function (Eq. 4) provided a better fitting quality  $(R^2 \ge 0.91$  for inact,  $R^2 \ge 0.93$  for operated), but when fit using a nonlinear least-squares minimization, the function was not continuous at the bone callus interface (Fig. 4c).

For both the intact and operated tibiae, the best fitting method was to use the multi-objective optimization method (Fig. 4d) to identify the parameters of the fitting function shown in Eq. 4 with constraints defined by Eq. 2. This produced continuous fit functions with goodness of fit statistics showing  $R^2 \ge 0.86$  for all 26 intact tibiae and  $R^2 \ge 0.88$  for all 26 operated tibiae. In all samples, all six fitting



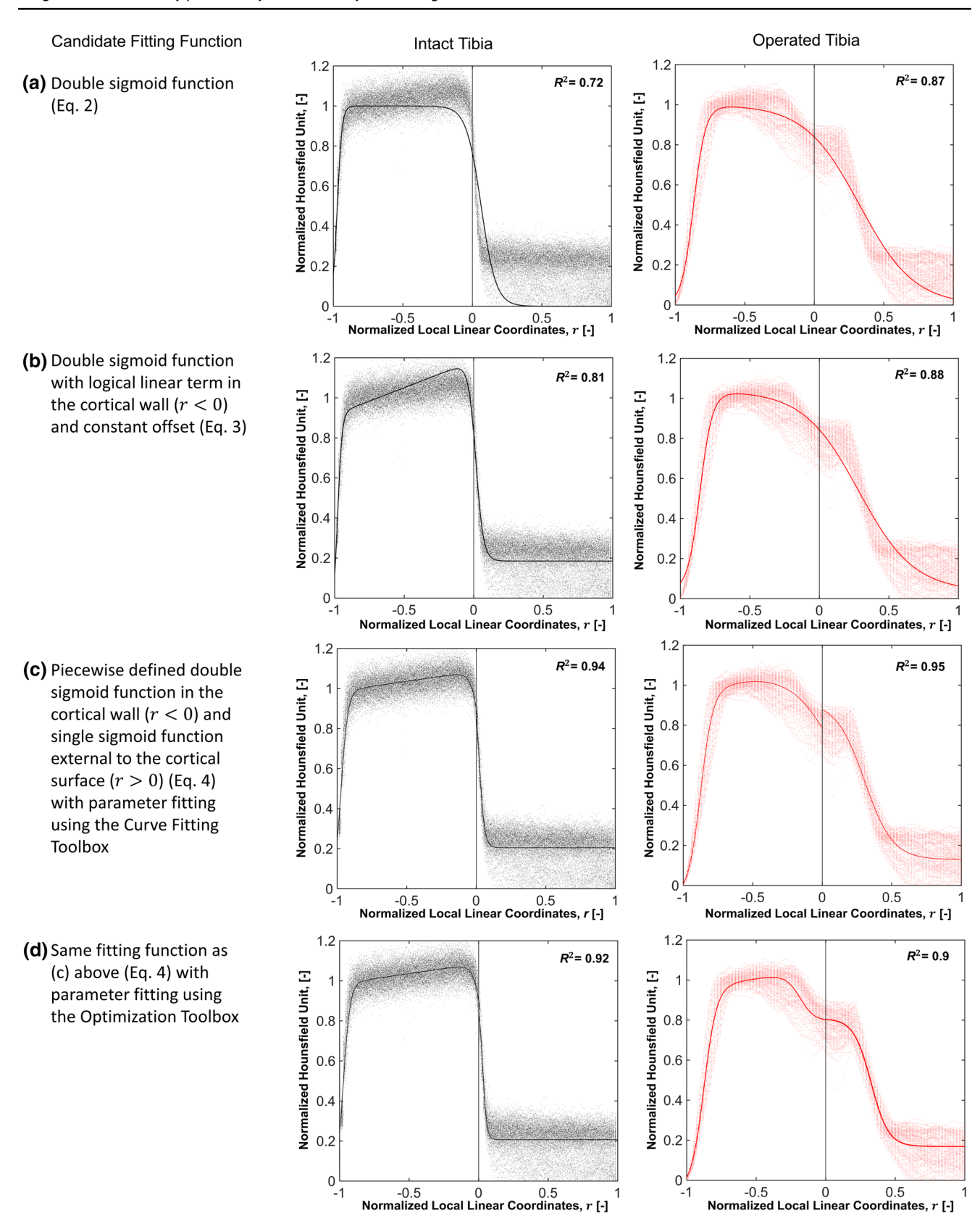
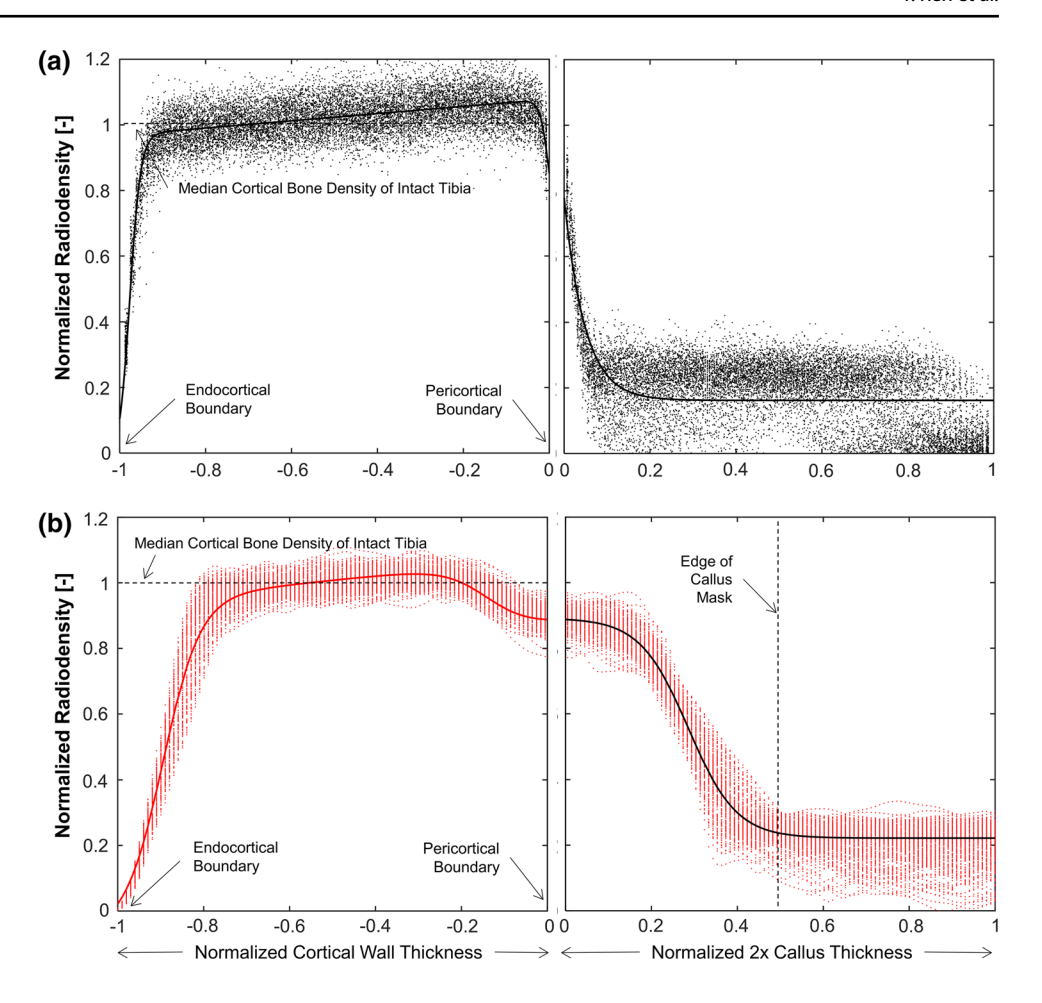


**Fig. 4** Profilometry data sampled at the level of the fracture for intact tibiae (black, left) and operated tibiae (red, right). Fit curves from the three tested fitting equations in panels (a)–(c), with all parameters obtained following a least-squares minimization approach using

the Curve Fitting Toolbox in MATLAB. Fit curves in panels (**c**) and (**d**) both use Eq. 4, but additional continuity constraint at r = 0 was achieved in (**d**) using multi-objective optimization



Fig. 5 Profilometry sampling points sampled at the midshaft of the intact tibia (a) and operated tibia (b) using the method of Fig. 4d in a different animal. The radial coordinate registration procedure allowed consistent referencing of key physical locations across different animals: endocortical boundary, pericortical boundary, and callus outer boundary (if present). The density normalization procedure eliminated baseline differences in bone properties between animals by scaling all sampling data points to the median cortical bone density for the intact tibia in each animal



parameters had 95% confidence intervals that did not include zero. The fitting parameters for all 26 animals at each of the six sampled ROIs can be seen in the Supplementary Table. Although the achieved  $R^2$  values were slightly lower with multi-objective optimization of Eq. 4 compared to the nonlinear least-squares method, the additional constraints introduced with Eq. 2 in the optimization-based method preserved the function's continuity at r = 0, which was highly desirable.

The performance of the final fitting function (Eq. 4 with multi-objective optimization constraints defined by Eq. 2) is shown for a different animal in Fig. 5. This single function successfully captured several observed characteristics of both the intact and operated limbs. Specifically, in the intact tibiae, it captured the observed increase in radiodensity in the radial direction from the endosteal to the pericortical boundary (Fig. 5a). For the operated limb, the fit curve captured the overall decrease in radiosity in the cortical wall and the localized remodeling at the pericortical boundary bounded by callus (Fig. 5b).

Each parameter of the fitting function was included to capture the observable features of the profilometry data in different regions of the fitted curve and at transitions between regions. The resulting constants can then be associated with

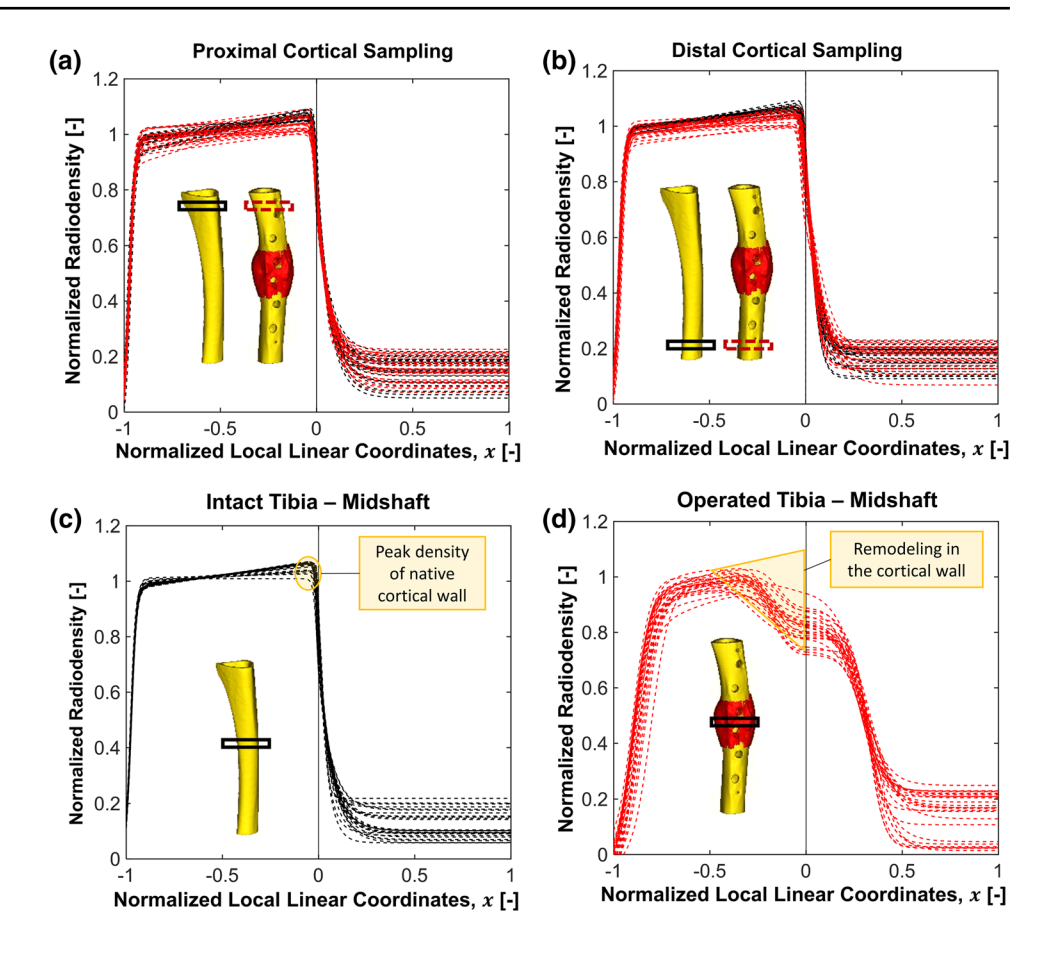
physical features related to the bone-callus radial density function. The magnitudes of parameters  $a_1$  and  $a_2$  define the width of the region of density change at the pericortical and endocortical boundaries of cortical bone. The parameters  $b_1$  and  $b_2$  define the location of the center of the transition of the pericortical and endocortical boundaries of cortical bone. Parameter  $a_3$  defines the width of the region of density change at the outer boundary of the callus, while parameter  $b_3$  sets the location of the center of the transition between callus and the surrounding soft tissue. The linear term c in the cortical bone zone  $(r \le 0)$  defines the increasing density of cortical bone from the endosteal to pericortical boundary. The constant  $d_1$  captures the average density of cortical bone and the term  $d_2$  compensates for the noise of the data outside the callus. Finally,  $g_1$  and  $g_2$  capture the cortical density at the pericortical boundary of the injured limb.

#### 3.2 Cortical tissue alterations in operated limbs

In addition to profilometry sampling at the level of the fracture, we also analyzed cortical bone at the proximal and distal ends of the diaphysis of the intact and operated limbs. The resulting profilometry curves of all animals combined are shown in Fig. 6. Comparing the operated group to their



Fig. 6 Profilometry curves were fitted from data sampled at the same levels at the proximal end (a) or distal end (b) end of intact tibiae (black curves) and operated tibiae (red curves). Profilometry curves were also fitted from data sampled at the midshaft of all intact tibiae (c, black curves) and operated tibiae (d, red curves)



matched intact tibiae at both the distal and proximal ends of the bones, there were several changes in the cortical walls of the operated tibiae, both at the level of the fracture and at the proximal and distal ends of the bone. Table 1 shows the comparisons between the operated and intact limbs based on two summary parameters derived from the fitting functions—density slope at the pericortical boundary and mean cortical wall density. Each parameter was evaluated at the proximal, midshaft, and distal ROIs in both the intact and operated limbs. Both parameters were significantly different between operated and intact for all ROIs, although the cortical density decreases in the operated limb were  $10\times$  larger at the midshaft than at the proximal and distal ends of the bone. Considering all animals, sampling at the proximal and

**Table 1** Comparison of profilometry curve fitting parameters between operated and contralateral groups

Location	Radiodensity profilom- etry parameters	Limb	Estimate	95% confidence interval (CI) of difference	p value
Proximal	Slope at Periosteal	Operated	$-7.65 \pm 0.34$	(-1.12; -0.737)	*0.003
	Surface $(r=0)$ [HU/-]	Contralateral	$-8.31 \pm 0.64$		
	Mean Cortical Wall	Operated	$3019 \pm 17.3$	(-61.3; -20.4)	*< 0.001
	Density $(r < 0)$ [HU]	Contralateral	$3073 \pm 14.5$		
Midshaft	Slope at Periosteal	Operated	$-0.063 \pm 0.002$	(6.91; 12.2)	*< 0.001
	Surface $(r=0)$ [HU/-]	Contralateral	$-12.1 \pm 0.16$		
	Mean Cortical Wall	Operated	$2718 \pm 8.71$	(-492; -445)	*< 0.001
	Density $(r < 0)$ [HU]	Contralateral	$3328 \pm 3.26$		
Distal	Slope at Periosteal	Operated	$-7.10 \pm 0.40$	(0.371; 3.44)	*0.010
	Surface $(r=0)$ [HU/-]	Contralateral	$-8.94 \pm 0.48$		
	Mean Cortical Wall	Operated	$3004 \pm 21.6$	(-91.2; -43.5)	*<0.001
	Density $(r < 0)$ [HU]	Contralateral	$3094 \pm 14.9$		

p values from Student's paired t test, significance at p < 0.05



distal ends of the bone showed that the mean cortical density was 1.3% and 2.2% lower, respectively, in the operated limbs compared to intact (p < 0.001).

All animals also showed evidence of remodeling in the cortical wall bounded by callus (Fig. 6d). The preexisting increase in radiodensity toward the pericortical boundary that can be seen in the intact bones (Fig. 6a) disappeared in the operated bones (Fig. 6c). At the pericortical boundary bounded by callus, these changes corresponded to a 23.4% drop on average from the peak density of the native cortical wall. Overall, comparing the intact and operated groups at the midshaft, there were statistically significant differences in all obtained radiodensity profile fitting function parameters except for  $g_1$  ( $p \le 0001$ ; see Supplementary Table S2). The slope of the fitted density profile curve at the pericortical boundary was also significantly reduced in operated limbs compared to intact at all three ROIs ( $p \le 0.007$ ; see Table S2). There were no significant differences in fit parameters sampled at the midshaft between animals with 3 mm osteotomies and 17 mm osteotomies (all p > 0.05; see Table S1 for fitting parameters in each animal).

#### 4 Discussion

This study presents a scalable mathematical method for noninvasive quantification of tissue mineralization density of the cortical tissue matrix and callus within an ovine tibial shaft. The results show that remodeling alterations occur not only in the callus tissue due to mineralization but also in the cortical tissue adjacent to the repair zone throughout the healing process. The findings are consistent with expectations from destructive physical testing and confirm the presence of a decreasing gradient in mineral density of the cortical bone at the vicinity of a fracture during secondary healing (Manjubala et al. 2009; Preininger et al. 2011). We previously showed that at sacrifice, most of these osteotomies had achieved a structural rigidity comparable to intact tibiae (Schwarzenberg et al. 2021a). This profilometry curve fitting data shows that in sheep, significant adaptive changes have occurred in cortical bone bounded by callus, concurrent with structural bridging as early as 9 or 12 weeks post-op. It should be noted that the remodeling of cortical bone was measurable not only near the fracture site, but also to a lesser extent at the proximal and distal end of the operated limbs. The methods described herein could be used to measure remodeling as a temporal in vivo outcome measure from imaging only. These measures could be useful as an indicator of healing speed by establishing the status of a fracture on the continuum of mechanical and structural adaptations that arise during healing. This technique could also be a valuable complement to existing microCT-derived quantitative measures such as cortical thickness, bone volume, and bone mineral density that are currently being used in animal models and clinical studies of diseases such as osteoporosis or osteogenesis imperfecta (Campbell and Sophocleous 2014; Seeman 2015; Molthen et al. 2016).

This study is also interesting because it suggests that contrary to popular opinion, remodeling is not an afterthought of fracture repair. In the literature, remodeling of woven bone is frequently described as the fourth and final stage of fracture healing, occurring for the purpose of resorbing the callus after bridging is complete (Marsell and Einhorn 2011; Loeffler et al. 2018; Bahney et al. 2019; Anani and Castillo 2021). This study reveals a second feature of remodeling—changes to the cortical wall—that occurs early in the healing process and may be independent of the progress of callus bridging. Support for this observation comes from our inclusion of both normal- and delayed-healing cases (3 mm gap and 17 mm gaps with autograft, respectively). In our previous work, we found that 17 mm gaps were notably slower to heal, having the lowest postmortem torsional rigidity even though the animals were sacrifice at 12 weeks rather than the standard 9 weeks for 3 mm gaps (Schwarzenberg et al. 2021a). Despite the slower rate of bridging, when we evaluated cortical remodeling just proximal to the osteotomy line using the profilometry data, we found no statistically significant differences in any of the remodeling parameters between the 3 mm and 17 mm animals. Despite their slower healing, animals in the 17 mm group experienced cortical remodeling on par with the 3 mm animals. This suggests that the cortical wall remodeling could be happening concurrently with the earliest stages of healing. Our scans were taken at a single timepoint only, so we cannot definitively establish the timeframe for initiation of cortical remodeling. However, our findings suggest that mechanistic studies focused on the timing and mechanobiological drivers of this effect may be warranted.

The intended purpose of this investigation was to provide a useful set of validation data for the future development of mechanoregulatory models that include the cortical wall and address coupled remodeling at the cortical-callus boundary. The results confirm that significant changes do occur on the cortical side of the cortical-callus boundary and that not addressing these changes is a critical limitation in the current computational models of bone fracture healing. These models usually assume a time-invariant value for cortical bone stiffness, which does not reflect the in vivo reality of a 23% drop in cortical radiodensity at the cortical-callus boundary. The normalized generalizable fitting function we reported could be used to assess whether mechanoregulatory models that include the cortical zone are capturing the appropriate magnitude of changes, and whether the distribution of predicted material properties at the boundary and within the callus region are valid.

Investigators who are interested in applying our normalized, dimensionless remodeling curve to validate their



dimensional mechanoregulation models may wish to use the following scaling procedure. First, observe that the fitting curve cannot be used directly because the function has been normalized in both the radius coordinates (r) and radiodensity values (y-axis). To dimensionalize the radial coordinates, recall that the radial coordinates were normalized to the cortical wall thickness for r < 0 and to the doubled callus thickness for r > 0. To scale this function appropriately in r, identify the cortical wall thickness, t, and callus thickness,  $t_c$ . The y coordinates in our fit curve were normalized to the median radiodensity [HU] of the intact limb for each animal. For the N=26 sheep analyzed in this study, the resulting average intact tibia radiodensity was  $3164 \pm 10$  HU. The apparent radiodensity [HU] must be scaled to bone mineral density by means of a linear conversion derived from a phantom scan. This density value can then be converted to a Young's modulus using a species-specific scaling law. For ovine cortical bone, we recommend the equation derived by Schwarzenberg et al. (2021b), which produces an average Young's modulus,  $E_{\rm intact} = 12.9$  GPa for intact bone. After selecting  $E_{\rm intact}$  and matching t and  $t_c$  to the chosen computational model, the following scaled remodeling function can be used to validate the model predictions:

medical images themselves could also influence the curve fitting quality. In this study, we have used high-resolution of micro-CT scans that were obtained post-mortem. Applying these same techniques to in vivo computed tomography would likely require larger voxel sizes and may not provide enough data points for curve fitting purpose in the area of transition especially at the cortical-callus boundary. We recommend that future studies explore whether larger voxels are inferior for detection of remodeling effects in the cortical wall.

# **5 Conclusions**

This study showed that structural remodeling at the bone-callus interface can be detected in sheep using radiodensity profilometry from micro-CT scans. It also showed that the density of cortical bone adjacent to callus, which correlates with its elastic properties, is not constant during the early healing period and that this region represents an integral part of the process of coupled fracture repair and remodeling. The scalable function presented herein for mathematically representing density gradients in the cortical wall and callus may be useful for validating future mechanoregulatory models of fracture repair.

$$E(r) = E_{\text{intact}} * \begin{cases} \left(\frac{1}{1 + e^{-a_1\left(\frac{r}{i} - b_1\right)}} * \left(g_1 + \frac{(1 - g_1)}{1 + e^{-a_2\left(\frac{r}{i} - b_2\right)}}\right) + \frac{rc}{t} + d_1\right), \ r < 0 \\ \left(\frac{g_2}{1 + e^{-a_3\left(\frac{r}{i} - b_3\right)}} + d_2\right), \end{cases} \qquad r \ge 0 \end{cases}$$

$$(5)$$

where the fitting constants  $(a_1, b_1, g_1, a_2, b_2, c, d_1, a_3, b_3, g_2, and d_2)$  are drawn from Table S1. This dimensionalized remodeling curve will have radial coordinates r that are zeroed at the cortical-callus boundary, but are dimensionally scaled to match the physical size of the geometry in the computational model.

This study is not without limitations. First, the sheep imaging data were only available at the time of sacrifice. As a result, no information about the temporal variations of local mechanical properties of the cortical tissue is currently available for this study. However, due to the inclusion of both large-gap and small-gap healing models, the selected sheep groups represent a wide range of healing responses and callus sizes, suggesting that the numerical methods and resulting fitting function we have proposed are robust. Another key limitation is that we applied the segmentation algorithm to evaluate only a small fraction of the 2D tomograms that comprise the entire cortical wall and focused on gradients in the radial direction. Remodeling effects in the cortical wall also have an axial dependency on proximity to the fracture line, which has not been explored here. Additional work would be required to achieve profilometry analysis of tissue density profiles in a more general 3D sense. Finally, it is important to note that the resolution of the Supplementary Information The online version contains supplementary material available at https://doi.org/10.1007/s10237-021-01553-2.

Acknowledgements The preclinical studies from which this data was obtained were funded by the Johnson & Johnson Family of Companies. The authors wish to thank Beat Lechmann (Johnson & Johnson Family of Companies) for agreeing to grant access to the ovine study data for our analyses. This material is based upon work supported by the National Science Foundation under Grant No. 1943287. Any opinions, findings, and conclusions or recommendations expressed in this material are those of the authors and do not necessarily reflect the views of the Johnson & Johnson Family of Companies or the National Science Foundation.

## **Declarations**

**Conflicts of interest** BvR is a paid consultant and receives research support as a principal investigator from Johnson & Johnson Family of Companies. The other authors report no conflicts relevant to this work.

#### References

Ament C, Hofer EP (2000) A fuzzy logic model of fracture healing. J Biomech 33:961–968. https://doi.org/10.1016/S0021-9290(00)00049-X
Anani T, Castillo AB (2021) Mechanically-regulated bone repair. Bone. https://doi.org/10.1016/j.bone.2021.116223



- Bahney CS, Zondervan RL, Allison P et al (2019) Cellular biology of fracture healing. J Orthop Res 37:35–50. https://doi.org/10.1002/ jor.24170
- Bissinger O, Götz C, Wolff KD et al (2017) Fully automated segmentation of callus by micro-CT compared to biomechanics. J Orthop Surg Res 12:1–9. https://doi.org/10.1186/s13018-017-0609-9
- Buie HR, Campbell GM, Klinck RJ et al (2007) Automatic segmentation of cortical and trabecular compartments based on a dual threshold technique for in vivo micro-CT bone analysis. Bone 41:505–515. https://doi.org/10.1016/j.bone.2007.07.007
- Campbell GM, Sophocleous A (2014) Quantitative analysis of bone and soft tissue by micro-computed tomography: applications to ex vivo and in vivo studies. Bonekey Rep 3:1–12. https://doi.org/10.1038/bonekey.2014.59
- Claes L, Eckert-Hübner K, Augat P (2002) The effect of mechanical stability on local vascularization and tissue differentiation in callus healing. J Orthop Res 20:1099–1105. https://doi.org/10.1016/ S0736-0266(02)00044-X
- Claes L, Recknagel S, Ignatius A (2012) Fracture healing under healthy and inflammatory conditions. Nat Rev Rheumatol 8:133–143. https://doi.org/10.1038/nrrheum.2012.1
- Einhorn TA, Gerstenfeld LC (2015) Fracture healing: mechanisms and interventions. Nat Rev Rheumatol 11:45–54. https://doi.org/10.1038/nrrheum.2014.164
- Engelhardt L, Niemeyer F, Christen P et al (2021) Simulating metaphyseal fracture healing in the distal radius. Biomechanics 1:29–42. https://doi.org/10.3390/biomechanics1010003
- Freedman BR, Rodriguez AB, Leiphart RJ et al (2018) Dynamic loading and tendon healing affect multiscale tendon properties and ECM stress transmission. Sci Rep 8:1–13. https://doi.org/10.1038/s41598-018-29060-y
- Ghiasi MS, Chen J, Vaziri A et al (2017) Bone fracture healing in mechanobiological modeling: a review of principles and methods. Bone Rep 6:87–100. https://doi.org/10.1016/j.bonr.2017.03.002
- Ghiasi MS, Chen JE, Rodriguez EK et al (2019) Computational modeling of human bone fracture healing affected by different conditions of initial healing stage. BMC Musculoskelet Disord 20:1–14. https://doi.org/10.1186/s12891-019-2854-z
- Isaksson H, Wilson W, van Donkelaar CC et al (2006) Comparison of biophysical stimuli for mechano-regulation of tissue differentiation during fracture healing. J Biomech 39:1507–1516. https://doi.org/ 10.1016/j.jbiomech.2005.01.037
- Lacroix D, Prendergast PJ (2002) A mechano-regulation model for tissue differentiation during fracture healing: analysis of gap size and loading. J Biomech 35:1163–1171. https://doi.org/10.1016/S0021-9290(02)00086-6
- Loeffler J, Duda GN, Sass FA, Dienelt A (2018) The metabolic microenvironment steers bone tissue regeneration. Trends Endocrinol Metab 29:99–110. https://doi.org/10.1016/j.tem.2017.11.008
- Manjubala I, Liu Y, Epari DR et al (2009) Spatial and temporal variations of mechanical properties and mineral content of the external callus during bone healing. Bone 45:185–192. https://doi.org/10.1016/j.bone.2009.04.249
- Marsell R, Einhorn TA (2011) The biology of fracture healing. Injury 42:551–555. https://doi.org/10.1016/j.injury.2011.03.031
- Molthen RC, Jameson J, Albert CI, Smith PA, Harris GF (2016) Role of micro-CT in the visualization, measurement, and quantification of bone structure in osteogenesis imperfecta. Shriners Hospitals for Children -Chicago, pp 195–216
- Mora-macías J, Pajares A, Miranda P et al (2017) Mechanical characterization via nanoindentation of the woven bone developed during bone transport. J Mech Behav Biomed Mater 74:236–244. https://doi.org/10.1016/j.jmbbm.2017.05.031
- Morgan E, Mason Z, Chien K, Pfeiffer A, Barnes G, Einhorn TGL, Morgan EF, Mason ZD et al (2009) Micro-computed tomography

- assessment of fracture healing: relationships among callus structure, composition, and mechanical function. Bone 44:335–344. https://doi.org/10.1016/j.bone.2008.10.039
- Pietsch M, Niemeyer F, Simon U et al (2018) Modelling the fracture-healing process as a moving-interface problem using an interface-capturing approach. Comput Methods Biomech Biomed Eng 21:512–520. https://doi.org/10.1080/10255842.2018.1487554
- Pivonka P, Dunstan CR (2012) Role of mathematical modeling in bone fracture healing. Bonekey Rep 1:1–10. https://doi.org/10.1038/ bonekey.2012.221
- Preininger B, Checa S, Molnar FL et al (2011) Spatial-temporal mapping of bone structural and elastic properties in a sheep model following osteotomy. Ultrasound Med Biol 37:474–483. https://doi.org/10.1016/j.ultrasmedbio.2010.12.007
- Ren T, Dailey HL (2020) Mechanoregulation modeling of bone healing in realistic fracture geometries. Biomech Model Mechanobiol. https:// doi.org/10.1007/s10237-020-01340-5
- Scheuren AC, Vallaster P, Kuhn GA et al (2020) Mechano-regulation of trabecular bone adaptation is controlled by the local in vivo environment and logarithmically dependent on loading frequency. Front Bioeng Biotechnol 8:1–13. https://doi.org/10.3389/fbioe.2020. 566346
- Schwarzenberg P, Klein K, Ferguson SJ et al (2021a) Virtual mechanical tests out-perform morphometric measures for assessment of mechanical stability of fracture healing in vivo. J Orthop Res 39:727–738. https://doi.org/10.1002/jor.24866
- Schwarzenberg P, Ren T, Klein K et al (2021b) Domain-independent simulation of physiologically relevant callus shape in mechanoregulated models of fracture healing. J Biomech. https://doi.org/10. 1016/j.jbiomech.2021.110300
- Seeman E (2015) Growth and age-related abnormalities in cortical structure and fracture risk. Endocrinol Metab 30:419–428. https://doi.org/10.3803/EnM.2015.30.4.419
- Shefelbine SJ, Augat P, Claes L, Simon U (2005) Trabecular bone fracture healing simulation with finite element analysis and fuzzy logic. J Biomech 38:2440–2450. https://doi.org/10.1016/j.jbiomech.2004. 10.019
- Simon U, Augat P, Utz M, Claes L (2011) A numerical model of the fracture healing process that describes tissue development and revascularisation. Comput Methods Biomech Biomed Eng 14:79–93. https://doi.org/10.1080/10255842.2010.499865
- Steiner M, Claes L, Ignatius A et al (2013) Prediction of fracture healing under axial loading, shear loading and bending is possible using distortional and dilatational strains as determining mechanical stimuli. J R Soc Interface. https://doi.org/10.1098/rsif.2013.0389
- Steiner M, Claes L, Ignatius A et al (2014) Disadvantages of interfragmentary shear on fracture healing—mechanical insights through numerical simulation. J Orthop Res 32:865–872. https://doi.org/ 10.1002/jor.22617
- Wang M, Yang N (2018) Three-dimensional computational model simulating the fracture healing process with both biphasic poroelastic finite element analysis and fuzzy logic control. Sci Rep 8:1–14. https://doi.org/10.1038/s41598-018-25229-7
- Wehner T, Steiner M, Ignatius A et al (2014) Prediction of the time course of callus stiffness as a function of mechanical parameters in experimental rat fracture healing studies—a numerical study. PLoS ONE 9:1–16. https://doi.org/10.1371/journal.pone.0115695
- Wilson CJ, Schütz MA, Epari DR (2017) Computational simulation of bone fracture healing under inverse dynamisation. Biomech Model Mechanobiol 16:5–14. https://doi.org/10.1007/s10237-016-0798-x
- **Publisher's Note** Springer Nature remains neutral with regard to jurisdictional claims in published maps and institutional affiliations.

